Journal of Colloid and Interface Science 606 (2022) 67–76

Contents lists available at ScienceDirect

Journal of Colloid and Interface Science

journal homepage: www.elsevier.com/locate/jcis

Elucidating the mechanism of dual-fluorescence in carbon dots

Jun-Ray Macairan [a,b], Tayline V. de Medeiros [a,b], Michela Gazzetto [c], Francisco Yarur Villanueva [a,b], Andrea Cannizzo [c,*], Rafik Naccache [a,b,*]

[a] Department of Chemistry and Biochemistry and the Centre for NanoScience Research, Concordia University, Montreal, QC H4B 1R6, Canada
[b] Quebec Centre for Advanced Materials, Concordia University, Montreal, QC H4B 1R6, Canada
[c] Institute of Applied Physics, University of Bern, Sidlerstrasse 5, CH-3012 Bern, Switzerland

GRAPHICAL ABSTRACT

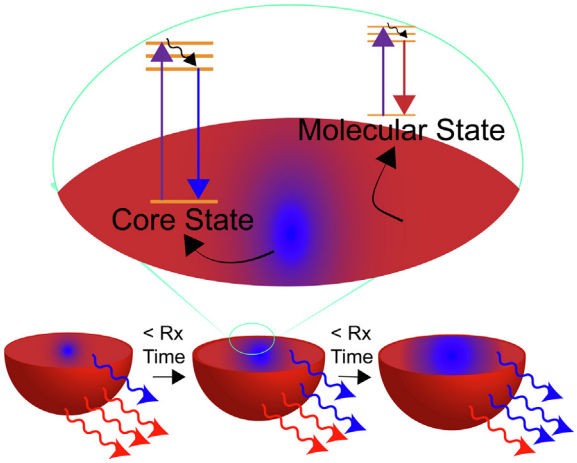

ARTICLE INFO

Article history:
Received 1 June 2021
Revised 23 July 2021
Accepted 31 July 2021
Available online 5 August 2021

Keywords:
Carbon dots
Fluorescence mechanism
Carbon-core
Molecular state
Optical properties

ABSTRACT

Carbon dots have garnered significant attention owing to their versatile and highly tunable optical properties; however, the origins and the underlying mechanism remains a subject of debate especially for dual fluorescent systems. Here, we have prepared carbon dots from glutathione and formamide precursors *via* a one-pot solvothermal synthesis. Steady state and dynamic techniques indicate that these dual fluorescent dots possess distinct emissive carbon-core and a molecular states, which are responsible for the blue and red optical signatures, respectively. To further glean information into the fluorescence mechanism, electrochemical analysis was used to measure the bandgaps of the two fluorescent states, while femtosecond transient absorption spectroscopy evidenced the two-state model based on the observed heterogeneity and bimodal spectral distribution. Our findings provide novel and fundamental insights on the optical properties of dual fluorescent dots, which can translate to more effective and targeted application development particularly in bioimaging, multiplexed sensing and photocatalysis.

* Corresponding authors at: Department of Chemistry and Biochemistry and the Centre for NanoScience Research, Concordia University, Montreal, QC H4B 1R6, Canada (R. Naccache); Institute of Applied Physics, University of Bern, Sidlerstrasse 5, CH-3012 Bern, Switzerland (A. Cannizzo).
E-mail addresses: andrea.cannizzo@iap.unibe.ch (A. Cannizzo), rafik.naccache@concordia.ca (R. Naccache).

https://doi.org/10.1016/j.jcis.2021.07.156
0021-9797/

1. Introduction

Carbon dots (CDs) are predominantly amorphous fluorescent nanoparticles comprising an sp^2/sp^3 carbon network with sizes spanning 10–15 nm. They are primarily composed of carbon, oxygen, hydrogen and nitrogen with the overall composition heavily dependent on the precursors and reaction conditions used. CDs are attractive owing to their facile and scalable synthesis from cheap and abundant precursors such as amino acids and sugars.[1-7] Interest in CDs has stemmed from the myriad of attractive electronic and optical properties, tunable features (size and surface chemistry), low photobleaching and photoblinking,[8,9] low toxicity and high chemical stability,[8,10,11] which are relevant to many applications including catalysis, bioimaging, sensing and drug delivery, among others.[12-16] Their tunable fluorescence can be tailored from the UV to the near-infrared (NIR); however, a significant knowledge gap persists in our fundamental understanding of how they actually fluoresce despite several well-founded works.[17-20]

Unlike quantum dots, CDs do not necessarily exhibit quantum confinement behavior. Instead, the optical properties are influenced by the composition of the surface and the core[21-23] as was demonstrated by Sciortino *et al*. who noted that the absence of blue-shifted fluorescence as a function of varying CD sizes.[24,25] CDs are conventionally considered to possess multiple emission centers, namely core and molecular states.[26-28] The former is dependent on the π-conjugated network at the carbogenic-core with a localized wavefunction, while the latter is dictated by the coupling of multiple functional groups at the surface with indications that the wavefunction delocalizes over the whole surface. Upon photoexcitation and as dictated by wavefunction overlap, electrons from the core state (HOMO) can transition to different LUMOs (i.e. core- or molecular- excited states); as a result, multiple fluorescence signatures can arise in a single particle. Song *et al*. also showed that fluorescence originated from both molecular states and carbon-core states with a CD-system based on citric acid and ethanolamine.[29] Through systematic studies, they determined that the formation of the CDs consisted of a highly fluorescent intermediate fluorophore, IPCA, and the carbon core. While the fluorescence core produced weak excitation-dependent fluorescence, the bound fluorophores were characterized by strong excitation independent fluorescence. This knowledge has led to the study of CDs for sensing applications by exploiting their reliable surface emission [28,30]. For instance, Yarur *et al.* demonstrated through metal quenching experiments that one of two fluorescence signals was quenched upon interaction with an analyte suggesting the presence of distinct states, namely core and molecular states [30]. However, other studies point to the fact that the fluorescence is dramatically influenced by the degree of crystallinity of the core, [23,31] or by the nature of the presence of free molecules in solution [32]. The existence of multiple hypotheses and mechanistic theories speaks to the need for extensive studies that can shed light and offer a better understanding of the optical properties of CDs.

Herein, we aim to further our fundamental understanding of the fluorescence mechanism of dual fluorescent CDs prepared from glutathione and formamide. Synthesis was carried out at different reaction times to study the evolution of the physical and optical properties, with careful purification to ensure removal of impurities and reaction intermediates. These nanoparticles possess unique optical properties with two distinct fluorescence signatures in different regions of the spectrum (blue and red), which are believed to originate from different emissive states. Steady state optical characterization highlights this unique property and evidences correlation between the length of the reaction time and the optical signature. We probe the fluorescence mechanism relying on electrochemical studies and femtosecond transient absorption spectroscopy. Our investigation of the dynamics of the photoexcited system reveals the presence of two prominent fluorescent centers and suggests a significant interplay between core and molecular states.

2. Experimental

2.1. Chemicals and reagents

Formamide (≥99.5%) and reduced L-glutathione (≥98.0%) were purchased from Thermo Scientific. All reagents (acetone, ethanol, acetonitrile, ferrocene and $TBAPF_6$) were used without further modification or purification.

2.2. Synthesis of carbon dots (CDs)

The CDs were synthesized *via* a hydrothermal-mediated reaction with glutathione and formamide. For each CD sample prepared at different times, a 20 mL solution of 0.1 M glutathione in formamide was prepared. The mixture was sonicated for 10 min until it changed from a cloudy to a clear homogeneous solution. The solution was transferred to a Teflon-lined container and placed inside a hydrothermal reactor. The reactor was heated at 180 °C at varying reaction times (1, 2, 4, 8 h). Once cooled, the dispersion was purified to remove excess unreacted materials and fluorophores via dialysis using a cellulose ester dialysis membrane (molecular weight cut-off = 3.5–5.0 kDa). The dialysis lasted for 5 days, with water being replaced twice a day. Following this step, the sample was concentrated down via rotovapping, and the remaining impurities were washed twice with acetone and ethanol (1:10, sample:solvent volume ratio; 10 min centrifugation at 10 000 G). The precipitate was collected after each wash. The final product was then dried in the oven at 70 °C overnight.

2.3. Characterization

2.3.1. Transmission electron microscopy

CDs were dispersed in water at a concentration of 5.0 mg/mL. Grids were prepared by pipetting 2 μL of the CD dispersion on a 300 Mesh Cu (Cu-300HD) coated with holey/thin carbon films (Grid-Tech) followed by evaporation of the solvent. The TEM images were collected using an LVEM5 benchtop electron microscope operating at 5 kV. Images were processed, and the carbon dot sizes were determined using Fiji imaging software.

2.3.2. UV–Vis absorbance spectroscopy

UV–visible absorption spectra were acquired from 200 to 800 nm on a Cary 5 Series UV–Vis-NIR Spectrophotometer (Agilent Technologies) using a 1 cm quartz cuvette. A 5.0 nm bandwidth and wavelength changeover at 450 nm were used for analysis. Data were processed using Cary Eclipse software.

2.3.3. Fluorescence quantum yield measurements

Quantum yield values were acquired on an FLS920 Fluorescence Spectrometer (Edinburgh Instruments) with an integrating sphere using a 1 cm quartz cuvette. The excitation and the emission slits were set to a width of 5 nm, and The excitation wavelength was set to 405 nm; the spectra from 300 to 800 nm were collected. The quantum yields of the blue and red component were taken in isolation; this is done by collecting the spectra from 300 to 550 nm (blue fluorescence) and 550–800 nm (red fluorescence).

Scans were done in triplicates with a dwell time of 0.25 *sec*. Data were processed using F900 Software.

2.3.4. Fluorescence spectroscopy

Fluorescence spectra were acquired using a Cary Eclipse fluorescence spectrophotometer (Agilent Technologies). Spectra were acquired in a 1-cm quartz cuvette at λ_{ex} = 405 nm. The excitation and emission slits were set to a width of 5 nm with a PMT voltage at 600 V. All data were processed using Cary Eclipse software.

2.3.5. Fourier-transform infrared spectroscopy (FT-IR)

Fourier-Transform Infrared Spectroscopy (FT-IR) spectra were collected using a Thermo Scientific Nicolet iS5 equipped with an iD5 ATR accessory. Spectra were collected using 30 scans with a resolution of 0.4 cm^{-1}, a gain of 1, an optical velocity of 0.4747 and an aperture setting of 100. Data were processed using Omnic 9 software.

2.3.6. X-ray photoelectron spectroscopy (XPS)

A Thermo Scientific K-Alpha X-Ray Photoelectron Spectrometer was used to obtain the XPS spectra of the CDs. Each analysis was carried out in triplicate with 10 runs for each scan and the averages were plotted for both the survey and high-resolution scans.

2.3.7. Cyclic voltammetry

Electrochemical measurements were performed using a Wave-Driver 200 Integrated Bipotentiostat/Galvanostat workstation. A three-electrode system was used to analyze the photoelectrochemical response of the different CDs with an FTO substrate as a working electrode (WE), a platinum wire as a counter electrode (CE), and a Ag wire as a reference electrode in a 0.1 M tetrabutylammonium hexafluorophosphate (TBAPF6) electrolyte solution. All potentials were measured against the reference electrode. The films of CDs on the FTO were illuminated by four white LEDs at a 5 cm distance from the film. The electrochemical properties of the CDs were determined using a three-electrode system by drop-casting the CDs on a 1 mm button platinum WE, a platinum wire as a CE, and an Ag wire pseudo-reference electrode in a 0.1 M TBAPF6 solution. All potentials were calibrated against ferrocene as an internal standard.

2.3.8. Transient absorption spectroscopy (TAS)

TA experiments were carried out upon excitation at 620 nm, 425 nm and 310 nm. The 620 nm, linearly polarized pump beam was generated from a non-collinear parametric amplifier (Topas-White, by Light Conversion), pumped with 800 nm pulses from a 5 kHz Ti:Sapphire fs regenerative amplifier (Coherent Legend). The laser source provided 130 fs full width half maximum (FWHM) pulses focused into a ~60 μm diameter spot (1/e2). The energy per pulse was set to 60 nJ. 425 nm and 310 nm linearly polarized pump beams were generated by frequency doubling in a b–BBO 850 nm and 620 nm beams, respectively, from a non–collinear parametric amplifier (TopasWhite, by Light Conversion), pumped with 800 nm pulses from a 5 kHz Ti:Sapphire fs regenerative amplifier (Coherent Legend). These beams consisted of 90 fs (FWHM) pulses and were focused into ~60 μm diameter spot (1/e2) with energy per pulse of 90 nJ. The probe was a white-light continuum generated by focusing a small fraction of the 800 nm Ti:sapphire laser output to a 5 mm thick CaF2 plate. The probe spot at the sample position was ~40 μm diameter (1/e2). Pump and probe beams were spatially overlapped at the sample position, and the pump delay with respect to the probe was controlled by a motorized delay stage. The pump and probe polarization was set to magic angle conditions to avoid contribution of rotational diffusion to the signal. The probe beam was dispersed after the sample with a prism and detected by a 512 pixel CCD camera (Hamamatsu S11105 Series) capable of measuring single-shots. A reference baseline for the pump/reference ratio was recorded for each measurement by introducing a mechanical chopper in the pump beamline at half the repetition rate to block every other pump pulse. A photo-diode after the chopper monitored the shot-to-shot pulse intensity to sort "pumped" and "unpumped" measurements and to compensate for fluctuations and drifts of the pump pulse intensity. To avoid photo-degradation, the sample solutions were flowed with a micro gear pump through a UV-grade quartz flow cell with an internal path length of 200 μm. Special care was taken to measure in linear regime in terms of pump and probe intensity and sample concentration. Typical signals were obtained by averaging 500 pumped and 500 unpumped spectra for each time delay and scanning over the pump–probe delay 5–10 times. Steady-state UV–visible absorption spectra measured before and after TA measurements showed no changes, indicating the remarkable photostability of the investigated complexes.

3. Results and discussion

CDs were synthesized at a temperature of 180 °C with varying reaction times from 1 to 8 h (See SI for experimental details) as shown in Scheme 1 and Fig. S1 (CD-1, CD-2, CD-4 and CD-8 corresponding to 1, 2, 4 and 8-hour reaction times). The size and the morphology of the dots were investigated using transmission electron microscopy (TEM). The TEM micrographs (Fig. S2a-d) indicate that the CDs are quasi-spherical with sizes ranging from 12 to 15 nm and an appreciable particle size overlap (Table S1). The XRD patterns present a broad amorphous halo spanning 10–80 °2θ, as observed for CD-1 (Fig. 1a),[30,33] yet with increasing reaction times, an increasingly crystalline profile is confirmed by the appearance of a crystalline reflection centered at 27.3° 2θ ascribed to the (1 0 0) diffraction plane of graphitic structures. This is attributed to an increase of the polymerization levels of the CDs and formation of more organized structures.[34]

Detailed XPS investigations into the composition and nature of the chemical bonds of the CDs (Fig. S3) confirm the presence of four peaks centered at 531 eV, 400 eV, 285 eV and 164 eV ascribed to the binding energies of O1s, N1s, C1s and S2p respectively. The deconvolution of the high-resolution XPS spectra (HR-XPS) of C1s (Fig. 1b-e) reveal binding energies ascribed to C—N (287.5 eV), C—O/C=O (285.9 eV) and C—C/C=C (284.6 eV) functional groups. The samples synthesized from 1 to 4 h present similar photoelectron spectra, however a slight increase in the C—O/C=O peak is observed with an increasing reaction time suggesting amide bond formation. The dots prepared at 8 h, however, present a major increase in the C—N and C=N peaks. This is attributed to the increase in carbonization at longer reaction times. Initially, precursors form highly fluorescent molecules; as the reaction progresses, reactants and fluorophores further carbonize to form the carbogenic core.[35] The HR-XPS for O1s (Figure S4) evidences C=O (532.2 eV) and C—O/C—OH (531.0 eV) functional groups for all CDs. An increase in the C—O/C=O peaks is observed from 1 to 4 h. However, at 8 h, most of the oxygen is present under the form of C=O. The HR-XPS for N1s (Fig. S5) indicates the presence of pyrrolic (399.6 eV) and pyridinic (398.17 eV) moieties. With the increasing reaction time, an increase in the peak of the pyridinic nitrogen is observed, indicating the formation of a larger aromatic domain. Lastly, the HR-XPS for S2p confirm the presence of S=O (167.9 eV), thiols (164.5 eV), and thiophenes (163.3 and 167.1 eV). With increasing reaction time, S=O groups are further oxidized giving rise to SO_x species.

We further investigated the surface chemistry of the dots, with increasing reaction times, *via* FTIR (Fig. 1f) and our findings corroborate the XPS results. For all four types of dots, we note a broad

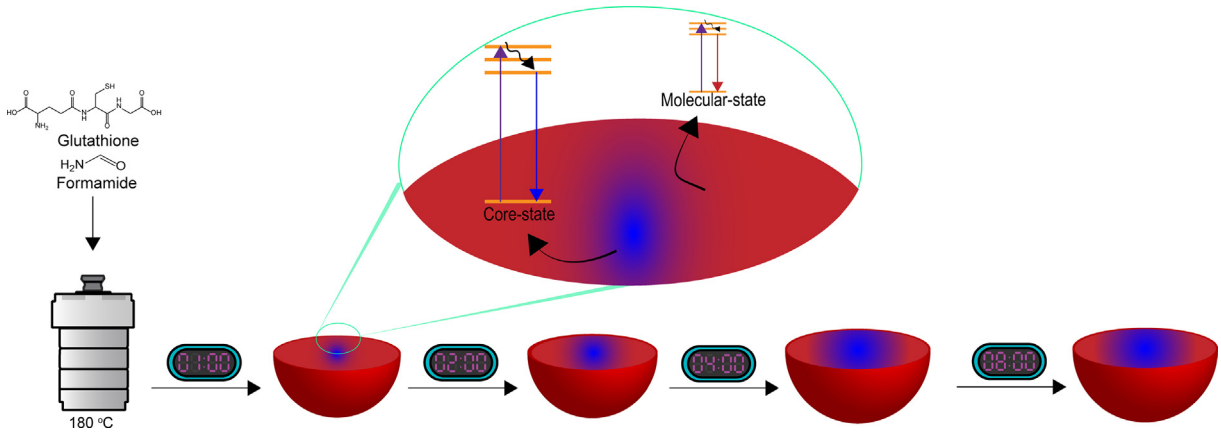

Scheme 1. Preparation of dual-fluorescent CDs with glutathione and formamide. The CDs were prepared via solvothermal assisted reaction at 180 °C with different reaction times. Such change in reaction parameters results in the CDs exhibiting different fluorescence signatures in both the blue and red regions of the spectrum, which stem from the core- and molecular-states, respectively. (For interpretation of the references to color in this figure legend, the reader is referred to the web version of this article.)

band ranging from 3500 to 3000 cm^{-1} ascribed to the symmetric and asymmetric stretching modes of the N—H and —OH groups, while stretching modes of amide C═O, C—OH and C—N were observed at 1671, 1596 and 1384 cm^{-1}, respectively. The similarities between the FT-IR and XPS spectra suggest that the changes in optical properties (*vide infra*) arise from structural modifications at the core, and the interface of the core and the surface of the dots; in other words, molecular states do not stem from a single surface functional group but rather delocalized throughout multiple functional groups.[24] We confirmed the increased carbonization of the CD core through Raman spectroscopy (Fig. 1g) where characteristic D (structural disorder) and G bands (graphitic order) at 1344 and 1525 cm^{-1}, respectively, were measured. The core of the CDs comprises sp^2 clusters, which are largely responsible for the G band. [22,36,37] It is noted that the I_D/I_G (intensity band ratio) decreases with increasing reaction time (from 1.19 for CD-1 down to 0.77 for CD-8) induced by the growth of the aromatic domain and the graphitization of the carbon-core of the CDs,[38] which induces a more ordered structure.

As shown in Fig. 2a, the UV–Vis absorption spectra of the samples display three analogous prominent bands at 320 nm, 400 nm and 580–700 nm. The first band is assigned to the transition of the C═C bonds of the carbon-core, while the second and third bands are ascribed to the $\pi \rightarrow \pi^*$ and $n \rightarrow \pi^*$ transitions of the aromatic sp^2 domains for the C═O and C═S/C═N, respectively.[26,30,39] The overall absorbance decreases with increasing reaction times; it is noted that the absorbance band intensities at 580–700 nm decrease at a faster rate than those in the lower regions of the spectrum. The multiple absorption bands emanate from different emissive

states, the first state being the carbon-core state comprising primarily an sp^2 carbon network, while the second corresponds to the molecular states.[36] As shown by XRD and XPS, an increase in reaction time further causes carbonization and aromatization. This, in turn, leads to the formation of more extensive sp^2 networks (resulting in a larger carbon core, discussed in the XRD and XPS data) to the detriment of the surface upon further carbonization. [18,19,40] This process inevitably modifies the local environment relating to the HOMO wavefunction. Therefore, the overlap between the HOMO and surface LUMO wavefunctions will be affected due to an increase in spatial distance. This change affects the oscillator strength of the transition resulting in a decrease in absorption – specifically in the red region of the spectrum. The distinct change in absorbance profiles relates to the noticeable difference in the color of the CD dispersions (Fig. S1).

Steady-state fluorescence spectra showcase signatures in both the blue and red regions of the spectrum for all the samples further speaking to the potential for existence of two fluorescence centers. The blue component is noted to be excitation dependent, while the red fluorescence is excitation independent (λ_{ex} = 680 nm); these are attributed to the carbon-core and molecular states respectively.[27] As shown in the photoluminescence excitation (PLE) spectra (Fig. S6a), a broad range of wavelengths can be used to excite these states. In addition, different states can be probed as the excitation wavelength is changed with notable differences in the blue and red fluorescence contributions (Fig. S6b for CD-1). Both carbon-core and molecular states are excited simultaneously at $\lambda_{exc} \leq 420$ nm with lower excitation wavelengths favoring a stronger blue fluorescence. Conversely, longer excitation wavelengths ($\lambda_{exc} \geq 600$ nm) allow for excitation of the lower HOMO-LUMO bandgap of the red fluorescence component band.

Steady state fluorescence studies suggest that apart of changes in spectral intensities of the blue and red emissions, which are indicative of the variations in accessible emissive centers, both bands evidence no changes in spectral shape (Fig. 2c). The relative red:blue fluorescence intensity is at its maximum for CD-1 and decreases with increasing reaction times (Fig. 2d). A similar trend is observed for fluorescence quantum yield (QY, Fig. 2e-f) with values of 5.3%, 4.9%, 2.8% and 4.4% for CD-1, CD-2, CD-4 and CD-8, respectively. Upon closer inspection, the blue fluorescence is noted to gradually increase from 1.1 to 3.5%; inversely, its red counterpart decreases from 4.2 to 0.9%. This observation can be explained by the carbonization of molecules linked to the CDs, (responsible for the molecular states - red fluorescence) at the expense of the growth of the sp^2 network in the core (responsible for the core states - blue fluorescence).

The existence of both states was further verified *via* photobleaching experiments as it can be associated with the presence of different emissive centers.[19] Following extended periods of UV exposure (λ_{ex} = 365 nm), the red component of CD-1 decreases at a much higher rate than the blue component (Fig. S7). Such behavior is expected as the blue fluorescence mainly stems from the direct electron-hole recombination in the carbon core states of the CDs. This agrees with previous reports showing that the carbon core-states of CDs typically emit at a lower wavelength, possess better photobleaching resistance, and much lower fluorescence QYs relative to molecular states.[41,42] Furthermore, two lifetimes of 4.6 ns and 0.6 ns were identified, suggesting multiple fluorescence centers. It is postulated that the longer fluorescence lifetime stems from the relaxation of the electrons from

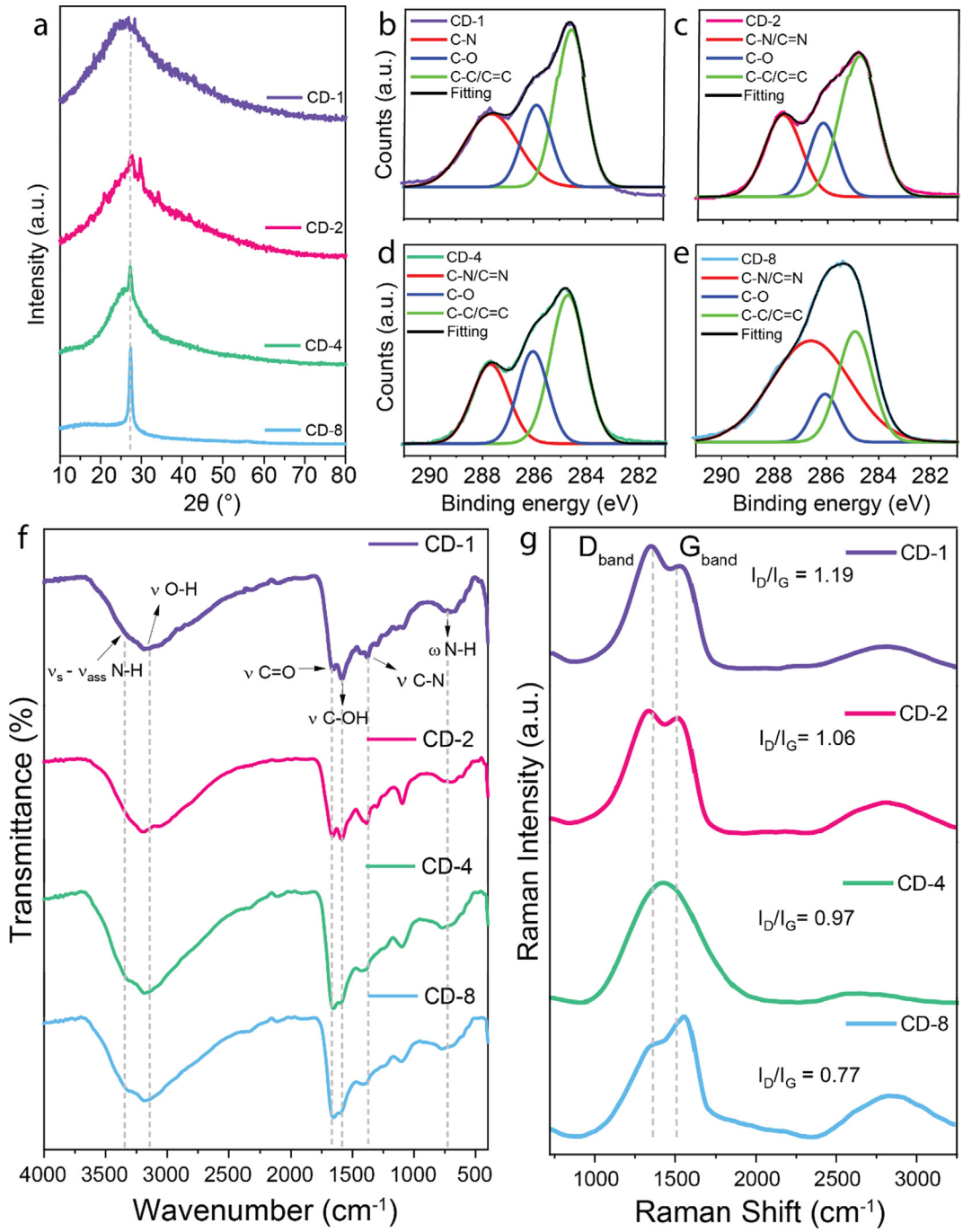

Fig. 1. (a) XRD patterns of CDs to evaluate their degree of crystallinity; HR-XPS of the C 1s spectrum for (b) CD-1, (c) CD-2, (d) CD-4 and (e) CD-8 illustrating the presence of C—N, C—O/C=O and C—C/C=C bonds (HR-XPS spectra for O1s, N1s and S2p are found in the Supplementary Information); (f) FT-IR spectra of the CDs showcasing the similarities in their surface functional groups; (g) Raman spectra of the CDs illustrating the increase in D/G bands ratio with increasing reaction times suggesting the growth of the aromatic core.

the core, while the fast lifetime corresponds to the electron-hole recombination in the molecular states.[43]

Our study of the optical properties in CDs has been influenced by previous investigations into the nature of the excitons in carbon nitride dots. However, it is important to recognize the disparities from our CD system to conceive a proper assignment of the optical transitions. The typical interpretation for the emissive centers in *N*-rich CDs is surface localized excitons. However, this explanation does not apply to our system because we observe differences regarding our optical data, despite having C=N sp^2 aromatic domains. For instance, carbon nitride dots show an emission peak at 525 nm (upon excitation at 410 nm).[44] Comparatively, we do not observe any significant emission under the same excitation regime.

Electrochemical and ultrafast transient absorption spectroscopy studies were carried out to probe the fluorescence dynamics. These investigations were limited to CD-1, as it provided the highest signal intensity for both red and blue fluorescence signatures. Cyclic voltammetry (CV) measurements were used to estimate the HOMO/LUMO energies of CD-1 Fig. 3a-b); all potentials reported were assigned against NHE. A non-reversible peak with an onset value of E_{ox} = +1.1 V was observed when the potential was swept

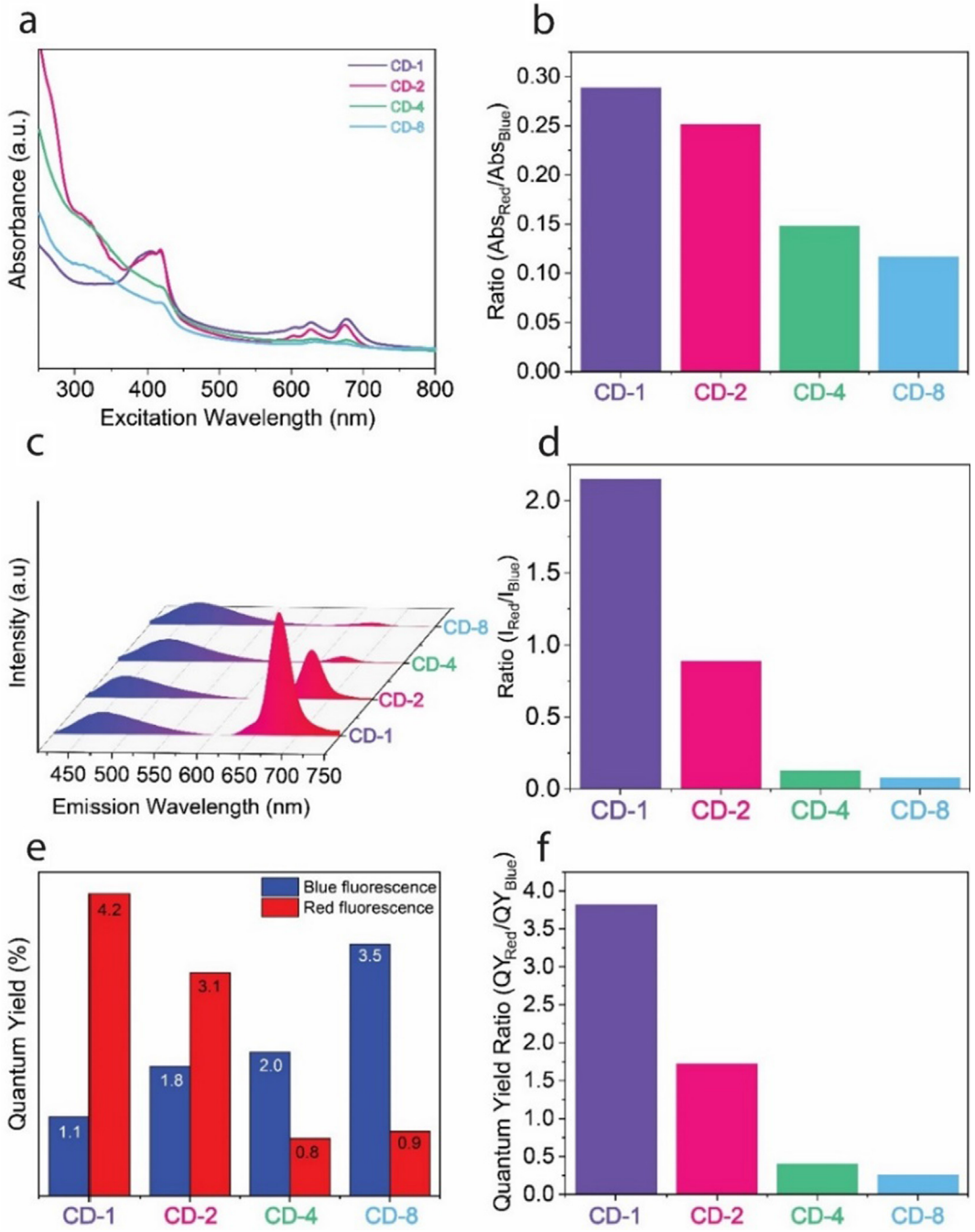

Fig. 2. UV–Vis absorbance and fluorescence spectra, and quantum yield of 50 μg mL^{-1}CD dispersion in MilliQ water; (a) UV–Vis absorption spectra of the CDs show three absorption bands centered at 320 nm, 420 nm and 580–700 nm; (c) Following excitation at 420 nm, two fluorescence bands are observed at 350–550 nm and 650–750 nm (spectra normalized to blue the fluorescence); (e) Quantum yield measurements of the blue and red fluorescence at an excitation wavelength of 420 nm. (b) The absorbance, (d) the fluorescence and (f) the quantum yield show a similar trend in which the signal of the red region of the spectra decreases relative to that in the blue. (For interpretation of the references to color in this figure legend, the reader is referred to the web version of this article.)

through the oxidative side (Fig. 3a). Likewise, another non-reversible wave was noted when the potential was swept through the reductive side with an onset value of E_{red} = −0.9 V. Interestingly, when comparing these values to the absorbance spectroscopy results, the HOMO-LUMO gap calculated from CV (2.0 eV) is in agreement with the UV–Vis data for the red component of the CDs dispersed in water (λ_{max} = 680 nm). To calculate the HOMO and LUMO of the blue component, blue fluorescent carbon dots were synthesized in a similar fashion for 20 h, completely removing the red fluorescence due to the excess carbonization.[30] The HOMO and LUMO were calculated to be −1.75 V and 1.2 V (Fig. 3b), respectively, which amounts to a band gap of 2.95 eV in accordance with the UV–Vis data for the blue fluorescence. As shown in Fig. 3c, this data suggests the possibility that the fluorescence stems from: (i) a direct electron-hole radiative recombination in each state (core and molecular) with (ii) the possibility of an energy transfer from the carbon core-state down to the molecular-state followed by a radiative recombination.

CD-1 were cast onto a transparent conductive substrate (FTO) to evaluate the photocurrent density at different excitation wave-

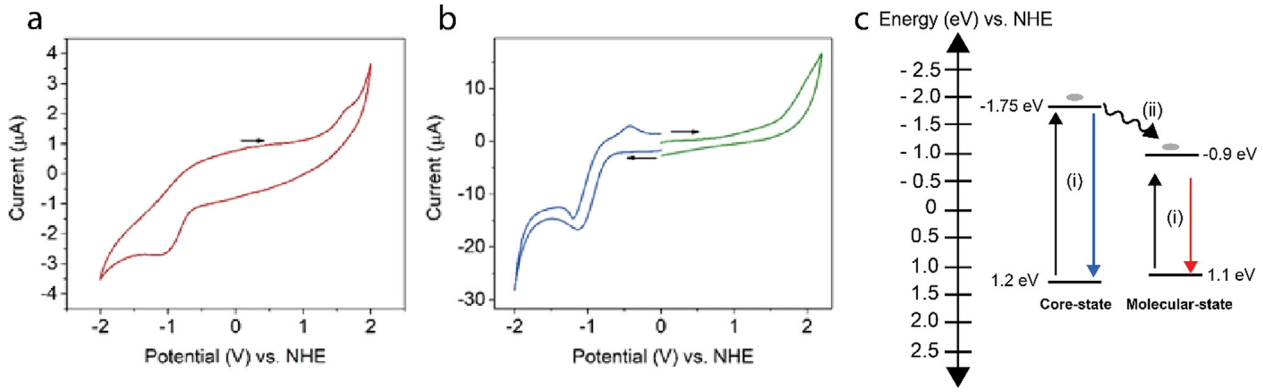

Fig. 3. Cyclic voltammograms for the calculation of the HOMO and LUMO positions for (a) CD-1 and (b) bCDs. The redox potentials for CD-1 were calculated from both the oxidative and reductive non-reversible peaks. These values were calculated from separate scans for bCDs. The oxidative potential was computed from the oxidative onset value (green scan), while the reductive potential was calculated from the non-reversible peak (blue scan). RE: Ag wire; CE: Pt wire; WE: FTO|CD-1 film, 0.1 M TBAPF6 in acetonitrile (Scan rate: 100 mV s^{-1}); (c) Simplified energy diagram representing the fluorescence stemming from the carbon core and molecular states. The HOMO and LUMO of both states are measured (1.2 eV and −1.75 eV for the core-state; 1.1 eV and −0.9 eV for the molecular state). Fluorescence stems from two possible pathways: (i) direct electron-hole radiative recombination and (ii) energy transfer of an excited electron in the core state to the molecular state followed by a radiative recombination. (For interpretation of the references to color in this figure legend, the reader is referred to the web version of this article.)

lengths through chronoamperometry in a three-electrode system with no applied bias. Three light sources were used including red (620–640 nm; λ_{max} = 630 nm), blue (455–475 nm; λ_{max} = 465 nm), and white LEDs (see white LED emission spectrum in Fig. S8); where the first two targets the red fluorescent component, while the white LEDs target both the blue and red together. Chopped-light illumination experiments were sequentially conducted with each light source cycling from white to red to blue for two cycles in a 0.1 M solution of $TBAPF_6$ with no sacrificial agents (Fig. S9). Upon irradiation, a current increase from the electron injection into the FTO was observed with a charging signature due to the build-up of charges at the solid–liquid interface. The current densities for all the chopped-light experiments were calculated and are shown Table S2. In addition, the integration of the absorption portion that is targeted by each LED was tabulated (Table S3) and compared to the current densities to correlate the density of states with the current output upon light irradiation. As expected, irradiation of the electrode with white light yields the highest current density since it can excite both the red and blue components of the dots (Fig. S8). The integration of the targeted absorption region for this excitation is also the highest. Interestingly, the red excitation yields Our results suggest that electrons responsible for the red fluorescence might populate the red excited state after a non-radiative electron transfer from the blue excited state (LUMO-LUMO transition), accounting for the high emission intensity for the red state compared to the blue when the sample is excited at 420 nm (Fig. 2c and Fig. S6). This electron transfer to the red state (or molecular state) can increase the current density observed in the chronoamperogram, which is what is observed when the CDs are irradiated use blue excitation wavelengths; this current density was almost comparable to that of the white excitation. Moreover, such behavior may point to the possibility that both emission signatures originate from the same ground-state located at the core of the CD, which is possible based on the similar calculated LUMOs.

Transient absorption spectroscopy (TAS) studies were carried out to investigate the dynamics of the optical processes. Colloidal CDs were excited at 620, 425 and 310 nm. Studies following excitation at 620 nm (Fig. 4a-c) investigate and isolate the electronic transitions for the red activity (RA; fluorescence at 680 nm). Conversely, excitation at 310 nm (Fig. 4d-f) provides information on the blue activity (BA; fluorescence at 475 nm). It is noted that CD-8 showed a very weak signal preventing its analysis. The TA spectra are compared to the steady state absorbance (Fig. 2a), fluorescence (Fig. 2c) and PLE spectra (Fig. S6), which enables the assignment of peaks to the following spectral features: (i) a negative ground state bleaching (GSB) due to a depopulation of the ground state following the pump absorption, which aligns with the peaks of the inverted absorption spectra; (ii) a negative stimulated emission (SE), where the shape would match the inverted fluorescence signal; (iii) a positive excited state absorption (ESA) due to transitions to higher energy levels. The TAS spectra evidence very few differences. At 620 nm (Fig. 4a-c), the spectra collected at the shortest observable time delays resemble closely inverted absorbance spectra with negative features (GSB) aligning with PLE at 680 nm. This confirms that these absorption bands share the same ground state, originating from the same chromophore, and are transitions to the first and second electronic excited states, leading to the red fluorescence at 680 nm. Within 10 ps, a prominent change in line-shape occurs, with a decay of a band centered at 390 nm, as well as a change in the GSB ratios at 640 and 680 nm (with the former decreasing rapidly) and the excited state absorption (ESA) at 450 nm disappears. The remaining signal is long-lived with ground state recovery in the ns timescale. This behavior is present in each sample (Fig. 4a-c) pointing towards the presence of two RA relaxation processes, each occurring at different timescales: (i) The first mechanism is on the order of a few ps and can be described by the decay of GSB at 390 nm and 640 nm, accompanied by the decay of the ESA at 450 nm and (ii) the second mechanism, responsible for the red steady-state emission, is slower and is assigned to the remaining ground state recovery signal, characterized by a GSB at 410 nm with a distinctive triangular shape and the SE at 680 nm. These results imply the presence of structural heterogeneity in the dots with multiple RA relaxation processes, involving different radiative and non-radiative channels. TAS experiments at 425 nm (Fig. S10) are consistent with the findings presented upon excitation at 620 nm. The overall signal and its evolution illustrate the slow decaying RA with a small contribution from the fast decaying RA, as would be expected from the excitation of the absorbance band presenting the higher quantum yield. A small SE rise at 680 nm for CD-1 and CD-2 can be observed at a short time scale of 140 to 460 fs (Fig. S10a-b). This is indicative of an ultrafast internal conversion from a higher excited state populating the lower excited states responsible for the red fluorescence.[45]

Time-resolved spectra following 310 nm excitation highlight transitions ascribed to BA (Fig. 4d-f). We note that the red component is still partially excited, based on the PLE in Fig. S6, preventing

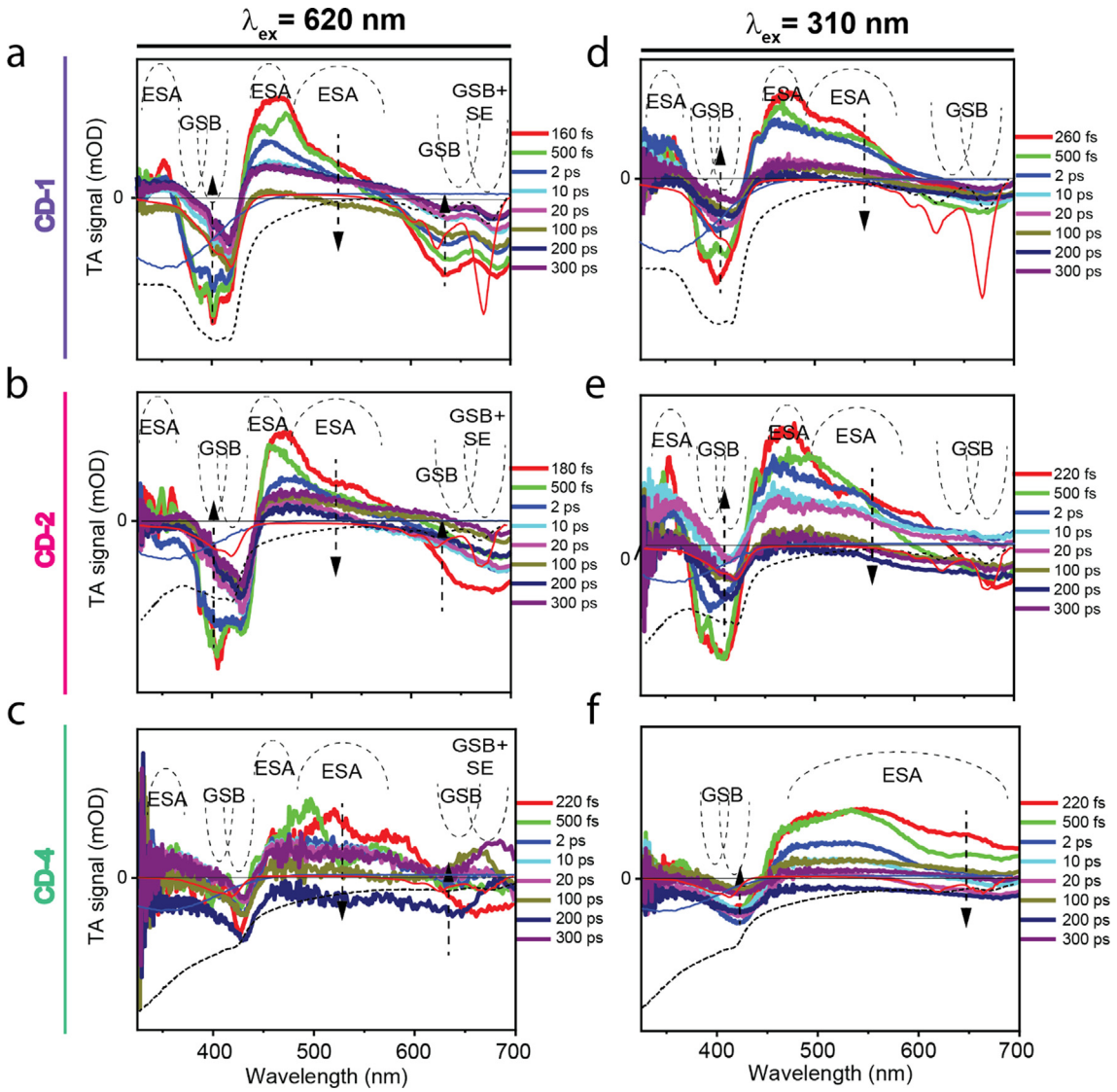

Fig. 4. Transient absorption (TA) spectra at selected delays of the CD-1, CD-2 and CD-4 (a-c) at l_{ex} = 620 nm and (d-f) λ_{ex} = 310 nm. The grey lines are guidelines to identify the different contributions to the TA signals: excited state absorption (ESA), ground state bleaching (GSB) and stimulated emission (SE). It's noted that the ESA contributions are always positive, while GSB and SE provide negative signals. The inverted absorbance spectra of the respective CDs are plotted in black (dashed); the inverted PLE for the PL at 475 nm and 680 nm are plotted in blue and in red, respectively. (For interpretation of the references to color in this figure legend, the reader is referred to the web version of this article.)

completely isolated studies of the blue counterpart. The main dynamics of the spectra at this excitation wavelength share similarities with the features observed using 620 nm excitation with some key differences: (i) The spectra at the shortest observable time delays are similar to the inverted absorbance spectra in the region between 350 nm and 600 nm; (ii) a reduction of the ESA peak at 450 with respect to broad ESA band at 500–550 was observed when compared to the signal at 620 nm excitation. This is expected as the blue fluorescence is absent upon excitation at 620 nm. The fact that we observe a reduction of the positive signal but not a change in sign of the overall signal (i.e. negative signal) means that the ESA is stronger than that of the stimulated emission; (iii) the GSB band at 620–640 nm exhibits a very weak signal, and GSB at 680 nm is much smaller relative to the GSB at 400 nm when compared to the experiment at 620 nm (Fig. 4a-c). Interestingly, a small rise of the signal up to 500 fs is observed, which suggests that there is still excitation of the red fluorescence (similar analyses at 425 nm). It cannot be conclusively discriminated here if, upon 310 nm excitation, the red activity is directly or indirectly populated from the energy states responsible for BA. This is due to a lack of evident signs of an energy transfer, apart from a small SE rise at 680 nm in the first 100 s fs, which in turn could stem from the excitation of the RA at higher energies. In the dynamics, we observe two mechanisms relating to RA: (i) a fast recovery at ps range, with the decay of GSB bands at 400 nm and 640 nm, accompanied by the decay of the ESA at 450 nm and (ii) a ground state recovery in the ns timescale. Interestingly, a major difference in the initial spectra is observed for the CD-4 sample (illustrated in Fig. 4f), where the presence of a broad ESA between 450 nm and 700 nm points to the excitation of electronic states in the molecular conduction band, consistent with the increase of the core crystalline structure. This evidence combined with the differences in the GSB could suggest the excitation of a transition with a different ground state with respect to the RA, with different initial and final excited states.

Our electrochemical and TAS results further supports that the multiple absorption bands (Fig. 2a) emanate from a typical HOMO localized at the core of the dot comprising primarily an sp^2 carbon

network. On a similar note, the blue and red fluorescence signals (Fig. 2c) are assigned to two physically distinct emissive states originating from a localized core LUMO and a delocalized molecular LUMO at the surface, responsible for the blue and red emission, respectively. In addition, our TAS data effectively disproves the presence of surface localized excitons, such as the ones observed in carbon nitride dots, because of the differences in the observed optical properties.[44] Instead, our results indicate a strong correlation with previous TAS studies on graphitic CDs.[46] To further our understanding of the fluorescence mechanism of these dots, it would be interesting to study the fluorescence anisotropy decay in the ultrafast and ns regime. This technique could give more insight relating to the blue and red activity, their origins and how they are coupled. In addition, the comparison of the two rotational relaxation times could provide vital information relating to the transitions of the different states found in the CDs.

4. Conclusion

As the fluorescence mechanism of CDs remains a topic of discussion, there remains an urgent need to generate novel and additional insights through various experimental studies to further our knowledge relating to this phenomenon. In this work, we synthesized a series of CDs using glutathione and formamide via a solvothermal reaction at varying reaction times. It is observed that these dots showcase a unique dual-fluorescence behavior where they concomitantly fluoresce in both the blue and red regions of the spectrum. The underlying mechanism of this dual-fluorescence phenomenon was investigated through extensive studies using steady-state and time-resolved fluorescence techniques. Our experimental results suggest that two emissive states are present: carbon-core and molecular states. The former stems from the sp^2 carbon network, while the latter originates from fluorophore-like moieties; the dual-fluorescence signature of these CDs is attributed to the presence of both states. We demonstrate that both excited states share the same ground state, based on the calculated HOMO/LUMO energies and the TAS studies. With this knowledge, we show that carbonizing the dot (i.e. increasing the reaction time) promotes a notable growth of the carbon-core sp^2 network allowing the decoupling of the distinct emissive states. Our results promote a better understanding of dual fluorescent CDs, and our iterative approach using synthesis and characterization offers novel insights into the design of CDs and tailoring their physico-optical properties.

CRediT authorship contribution statement

Jun-Ray Macairan: Conceptualization, Writing – original draft, Writing – review & editing, Formal analysis, Methodology, Investigation, Visualization, Validation. **Tayline V. Medeiros:** Writing – original draft, Writing – review & editing, Investigation, Formal analysis, Methodology, Visualization. **Michela Gazzetto:** Writing – original draft, Investigation, Formal analysis. **Francisco Yarur Villanueva:** Writing – original draft, Writing – review & editing, Investigation, Formal analysis. **Andrea Cannizzo:** Supervision, Writing – review & editing. **Rafik Naccache:** Supervision, Writing – review & editing.

Declaration of Competing Interest

The authors declare that they have no known competing financial interests or personal relationships that could have appeared to influence the work reported in this paper.

Acknowledgements

The authors would like to acknowledge funding sources for financial support for this research. RN is grateful to NSERC and FRQNT for funding. RN is also grateful to Concordia University and the Quebec Centre for Advanced Materials for financial support. TM acknowledges CAPES for the scholarship. TEM work was performed in Centre (CM)2 at McGill University with the assistance of Mrs. Mohini Ramkaran. XPS studies were performed at McGill University (MIAM Facilities in the Department of Mining and Materials Engineering) with the assistance of Dr. Lihong Shang. The authors acknowledge Ms. Vivian Andrade Luciano for her assistance with the Raman analysis.

References

[1] J. Jiang, Y. He, S. Li, H. Cui, Amino acids as the source for producing carbon nanodots: microwave assisted one-step synthesis, intrinsic photoluminescence property and intense chemiluminescence enhancement, Chem. Commun. 48 (77) (2012) 9634–9636.
[2] S. Cailotto, E. Amadio, M. Facchin, M. Selva, E. Pontoglio, F. Rizzolio, P. Riello, G. Toffoli, A. Benedetti, A. Perosa, Carbon dots from sugars and ascorbic acid: role of the precursors on morphology, properties, toxicity, and drug uptake, ACS Med. Chem. Lett. 9 (8) (2018) 832–837.
[3] H. Peng, J. Travas-Sejdic, Simple aqueous solution route to luminescent carbogenic dots from carbohydrates, Chem. Mater. 21 (23) (2009) 5563–5565.
[4] H.-J. Cheng, C.-L. Kao, Y.-F. Chen, P.-C. Huang, C.-Y. Hsu, C.-H. Kuei, Amino acid derivatized carbon dots with tunable selectivity as logic gates for fluorescent sensing of metal cations, Microchim. Acta 184 (9) (2017) 3179–3187.
[5] Z. Wang, B. Fu, S. Zou, B.o. Duan, C. Chang, B. Yang, X. Zhou, L. Zhang, Facile construction of carbon dots *via* acid catalytic hydrothermal method and their application for target imaging of cancer cells, Nano Res. 9 (1) (2016) 214–223.
[6] S. Chahal, N. Yousefi, N. Tufenkji, Green synthesis of high quantum yield carbon dots from phenylalanine and citric acid: role of stoichiometry and nitrogen doping, ACS Sustainable Chem. Eng. 8 (14) (2020) 5566–5575.
[7] J.-R. Macairan, I. Zhang, A. Clermont-Paquette, R. Naccache, D. Maysinger, Ratiometric pH sensing in living cells using carbon dots, Part. Part. Syst. Charact. 37 (1) (2020) 1900430, https://doi.org/10.1002/ppsc.v37.110.1002/ppsc.201900430.
[8] S.Y. Lim, W. Shen, Z. Gao, Carbon quantum dots and their applications, Chem. Soc. Rev. 44 (1) (2015) 362–381.
[9] S. Hu, A. Trinchi, P. Atkin, I. Cole, Tunable photoluminescence across the entire visible spectrum from carbon dots excited by white light, 54(10) (2015) 2970–2974.
[10] H. Li, Z. Kang, Y. Liu, S.-T. Lee, Carbon nanodots: synthesis, properties and applications, J. Mater. Chem. 22 (46) (2012) 24230–24253.
[11] M. Tuerhong, Y. Xu, X.-B. Yin, Review on carbon dots and their applications, Chinese J. Anal. Chem. 45 (1) (2017) 139–150.
[12] P.G. Luo, S. Sahu, S.-T. Yang, S.K. Sonkar, J. Wang, H. Wang, G.E. LeCroy, L. Cao, Y.-P. Sun, Carbon "quantum" dots for optical bioimaging, J. Mater. Chem. B 1 (16) (2013) 2116–2127.
[13] M.L. Liu, B.B. Chen, C.M. Li, C.Z. Huang, Carbon dots: synthesis, formation mechanism, fluorescence origin and sensing applications, Green Chem. (2019).
[14] S.N. Baker, G.A. Baker, Luminescent carbon nanodots: emergent nanolights, Angew. Chem. Int. Ed. 49 (38) (2010) 6726–6744.
[15] T.V. de Medeiros, J. Manioudakis, F. Noun, J.-R. Macairan, F. Victoria, R. Naccache, Microwave-assisted synthesis of carbon dots and their applications, J. Mater. Chem. C 7 (24) (2019) 7175–7195.
[16] K. Hola, Y.u. Zhang, Y.u. Wang, E.P. Giannelis, R. Zboril, A.L. Rogach, Carbon dots—emerging light emitters for bioimaging cancer therapy and optoelectronics, Nano Today 9 (5) (2014) 590–603.
[17] S. Zhu, Q. Meng, L. Wang, J. Zhang, Y. Song, H. Jin, K. Zhang, H. Sun, H. Wang, B. Yang, Highly photoluminescent carbon dots for multicolor patterning, sensors, and bioimaging, Angew. Chem., Int. Ed. 52 (14) (2013) 3953–3957.
[18] Y. Hu, J. Yang, J. Tian, J.-S. Yu, How do nitrogen-doped carbon dots generate from molecular precursors? An investigation of the formation mechanism and a solution-based large-scale synthesis, J. Mater. Chem. B 3 (27) (2015) 5608–5614.
[19] M. Shamsipur, A. Barati, A.A. Taherpour, M. Jamshidi, Resolving the multiple emission centers in carbon dots: from fluorophore molecular states to aromatic domain states and carbon-core states, J. Phys. Chem. Lett. 9 (15) (2018) 4189–4198.
[20] A.B. Bourlinos, R. Zbořil, J. Petr, A. Bakandritsos, M. Krysmann, E.P. Giannelis, Luminescent surface quaternized carbon dots, Chem. Mater. 24 (1) (2012) 6–8.
[21] H.A. Nguyen, I. Srivastava, D. Pan, M. Gruebele, Unraveling the fluorescence mechanism of carbon dots with sub-single-particle resolution, ACS Nano 14 (5) (2020) 6127–6137.
[22] M.C. Ortega-Liebana, N.X. Chung, R. Limpens, L. Gomez, J.L. Hueso, J. Santamaria, T. Gregorkiewicz, Uniform luminescent carbon nanodots prepared by rapid pyrolysis of organic precursors confined within nanoporous templating structures, Carbon 117 (2017) 437–446.

[23] M.O. Dekaliuk, O. Viagin, Y.V. Malyukin, A.P. Demchenko, Fluorescent carbon nanomaterials: "quantum dots" or nanoclusters?, Phys Chem. Chem. Phys. 16 (30) (2014) 16075–16084.
[24] A. Sciortino, A. Cayuela, M.L. Soriano, F.M. Gelardi, M. Cannas, M. Valcárcel, F. Messina, Different natures of surface electronic transitions of carbon nanoparticles, Phys. Chem. Chem. Phys. 19 (34) (2017) 22670–22677.
[25] A. Sciortino, M. Gazzetto, G. Buscarino, R. Popescu, R. Schneider, G. Giammona, D. Gerthsen, E.J. Rohwer, N. Mauro, T. Feurer, A. Cannizzo, F. Messina, Disentangling size effects and spectral inhomogeneity in carbon nanodots by ultrafast dynamical hole-burning, Nanoscale 10 (32) (2018) 15317–15323.
[26] L. Pan, S. Sun, L. Zhang, K. Jiang, H. Lin, Near-infrared emissive carbon dots for two-photon fluorescence bioimaging, Nanoscale 8 (39) (2016) 17350–17356.
[27] S. Zhu, Y. Song, X. Zhao, J. Shao, J. Zhang, B. Yang, The photoluminescence mechanism in carbon dots (graphene quantum dots, carbon nanodots, and polymer dots): current state and future perspective, Nano Res. 8 (2) (2015) 355–381.
[28] Y. Song, S. Zhu, S. Xiang, X. Zhao, J. Zhang, H. Zhang, Y. Fu, B. Yang, Investigation into the fluorescence quenching behaviors and applications of carbon dots, Nanoscale 6 (9) (2014) 4676–4682.
[29] L. Shi, J.H. Yang, H.B. Zeng, Y.M. Chen, S.C. Yang, C. Wu, H. Zeng, O. Yoshihito, Q. Zhang, Carbon dots with high fluorescence quantum yield: the fluorescence originates from organic fluorophores, Nanoscale 8 (30) (2016) 14374–14378.
[30] F. Yarur, J.-R. Macairan, R. Naccache, Ratiometric detection of heavy metal ions using fluorescent carbon dots, Environ. Sci.: Nano 6 (4) (2019) 1121–1130.
[31] A. Sciortino, E. Marino, B.V. Dam, P. Schall, M. Cannas, F. Messina, Solvatochromism unravels the emission mechanism of carbon nanodots, J. Phys. Chem. Lett. 7 (17) (2016) 3419–3423.
[32] M. Righetto, A. Privitera, I. Fortunati, D. Mosconi, M. Zerbetto, M.L. Curri, M. Corricelli, A. Moretto, S. Agnoli, L. Franco, R. Bozio, C. Ferrante, Spectroscopic insights into carbon dot systems, J. Phys. Chem. Lett. 8 (10) (2017) 2236–2242.
[33] J. Joseph, A.A. Anappara, Ellagic acid-functionalized fluorescent carbon dots for ultrasensitive and selective detection of mercuric ions *via* quenching, J. Lumin. 192 (2017) 761–766.
[34] A. Pal, M.P. Sk, A. Chattopadhyay, Recent advances in crystalline carbon dots for superior application potential, Materials Advances 1 (4) (2020) 525–553.
[35] Y. Song, S. Zhu, S. Zhang, Y. Fu, L. Wang, X. Zhao, B. Yang, Investigation from chemical structure to photoluminescent mechanism: a type of carbon dots from the pyrolysis of citric acid and an amine, J. Mater. Chem. C 3 (23) (2015) 5976–5984.
[36] S.K. Misra, I. Srivastava, J.S. Khamo, V.V. Krishnamurthy, D. Sar, A.S. Schwartz-Duval, J.A.N.T. Soares, K. Zhang, D. Pan, Carbon dots with induced surface oxidation permits imaging at single-particle level for intracellular studies, Nanoscale 10 (39) (2018) 18510–18519.
[37] E. Dervishi, Z. Ji, H. Htoon, M. Sykora, S.K. Doorn, Raman spectroscopy of bottom-up synthesized graphene quantum dots: size and structure dependence, Nanoscale 11 (35) (2019) 16571–16581.
[38] K. Hola, A.B. Bourlinos, O. Kozak, K. Berka, K.M. Siskova, M. Havrdova, J. Tucek, K. Safarova, M. Otyepka, E.P. Giannelis, R. Zboril, Photoluminescence effects of graphitic core size and surface functional groups in carbon dots: COO− induced red-shift emission, Carbon 70 (2014) 279–286.
[39] J.-R. Macairan, D.B. Jaunky, A. Piekny, R. Naccache, Intracellular ratiometric temperature sensing using fluorescent carbon dots, Nanoscale Adv. 1 (1) (2019) 105–113.
[40] P.-C. Hsu, H.-T. Chang, Synthesis of high-quality carbon nanodots from hydrophilic compounds: role of functional groups, Chem. Commun. 48 (33) (2012) 3984–3986.
[41] L. Bao, Z.-L. Zhang, Z.-Q. Tian, L. Zhang, C. Liu, Y. Lin, B. Qi, D.-W. Pang, Electrochemical tuning of luminescent carbon nanodots: from preparation to luminescence mechanism, Adv. Mater. 23 (48) (2011) 5801–5806.
[42] W. Wang, C. Damm, J. Walter, T.J. Nacken, W. Peukert, Photobleaching and stabilization of carbon nanodots produced by solvothermal synthesis, Phys. Chem. Chem. Phys. 18 (1) (2016) 466–475.
[43] V. Nguyen, J. Si, L. Yan, X. Hou, Electron–hole recombination dynamics in carbon nanodots, Carbon 95 (C) (2015) 659–663.
[44] M. Gazzetto, A. Sciortino, M. Nazari, E. Rohwer, G. Giammona, N. Mauro, T. Feurer, F. Messina, A. Cannizzo, Photocycle of excitons in nitrogen-rich carbon nanodots: implications for photocatalysis and photovoltaics, ACS Appl. Nano Mater. 3 (7) (2020) 6925–6934.
[45] J.R. Lakowicz, Principles of Fluorescence Spectroscopy, Second edition., Kluwer Academic/Plenum, New York, 1999. ©19991999.
[46] A. Sciortino, M. Gazzetto, M.L. Soriano, M. Cannas, S. Cárdenas, A. Cannizzo, F. Messina, Ultrafast spectroscopic investigation on fluorescent carbon nanodots: the role of passivation, Phys. Chem. Chem. Phys. 21 (30) (2019) 16459–16467.